Research Article

Mechanical and Electroconductivity Properties of Graphite Tailings Concrete

Hongbo Liu,[1,2] Ben Li [iD],[1,3] Jing Xue,[1] Jiayu Hu,[3] and Jing Zhang[1]

[1]*School of Civil Engineering, HeilongJiang University, Harbin 150080, China*
[2]*Ministry of Education of the People's Republic of China, Key Laboratory of Functional Inorganic Material Chemistry, Harbin 150080, Heilongjiang, China*
[3]*Advanced and Sustainable Infrastructure Materials Group, School of Transportation, Civil Engineering and Architecture, Foshan University, Foshan, Guangdong 528000, China*

Correspondence should be addressed to Ben Li; sktm1@163.com

This paper investigated the mechanical and electroconductivity properties of graphite tailings concrete, in which the graphite tailings are replaced as sand. The results showed that the concentration of graphite tailings has an important influence on the mechanical, electroconductivity, and material properties of concrete. Finally, a new model for calculating the relationship between compressive strength and electrical resistivity based on the grey correlation method was obtained for providing a theoretical basis for building green and intelligent building materials.

1. Introduction

The environmental impact of mineral solid waste is slow and long-term accumulation [1–8]. For a long time, treatment on mineral solid waste has not received enough attention, which has led to the relatively lagging development of the treatment of mineral solid waste in various subsectors in the field of environmental protection [9–16]. After several years of mining, the mine has produced a cumulative accumulation of tailings, which cause continuous unrecoverable damage and pollution to the environment [17–19]. With the implementation of China's "Environmental Protection Tax Law" and "Guidelines for the Construction of Solid Mineral Green Mines" in 2018, it is also an inevitable choice for mining enterprises to take the road of green mine construction. This requires higher standards and requirements for green treatment and comprehensive utilization of mine tailings solid waste. The solid waste generated from the development of mineral resources is collectively referred to as "*tailings*" such as iron tailings, copper tailings, and coal tailings, which have silicate properties and contain iron

oxide or aluminium oxide [20–22]. The treatment and comprehensive utilization of mine tailings have always been an international problem and listed as a major pollution problem with the disposal and reuse of construction waste.

Among these problems, graphite tailings for the green treatment and comprehensive utilization of waste management are increasingly being valued. Graphite, a significant resource in the 21st century, is mainly distributed in China, India, and Brazil. In 2017, the global graphite mine production was approximately 0.15 billion tons. China is a large country in the production of graphite ore, and the basic reserves of graphite deposits account for 43% of the world (81-million-ton cumulative production in 2017) and are mainly distributed in 14 ore veins in six provinces. However, mining 1-ton graphite mine produces 10 to 15 tons of graphite tailings. Years of mining have led to the accumulation of solid waste from graphite tailings, resulting in environmental degradation and soil erosion around the mine. The hazards of graphite tailings are gaining recognition, and the green treatment and comprehensive utilization of it are becoming a research hotspot in this field at

this stage. The use of graphite tailings for the preparation of building materials is a common means of greening, which can not only effectively exert the advantages of mineral solid waste, but also reduce the consumption of construction sand by a certain amount. Liu et al. [23–25] conducted a series of studies on the mechanical properties and electrical modification of graphite tailings concrete in which graphite tailings were replaced as sand used in concrete. Kathirvel et al. [26] studied the mechanical characteristics and electrochemical properties of graphite tailings reinforced concrete and mortar with different incorporation amount. Although a number of published literatures on concrete containing GT as sand have comprehensively evaluated the macroscopic properties of concrete, a comprehensive understanding and research is still at a preliminary stage. Simultaneously, there is no research on the influence of GT on the mesocharacteristics and electrical properties of cement-based materials, which has an important influence on the load-electric conversion relationship in the intelligentization of building materials and structures.

The present study is conducted to fill these research gaps by investigating the macroproperties, such as mechanical and electroconductivity properties, and mesoscopic morphology or pore structure distribution of GTC. Then, a new model based on grey relational degree theory was determined for evaluating compressive strength or electroconductivity properties of GTC. Finally, the relationship between mechanical properties and resistivity is investigated, which can provide theoretical support for the application of GT replacing as sand for the preparation of green and intelligent building materials.

2. Materials and Experimental Details

2.1. Materials

2.1.1. Raw Materials and Mixing Proportions. Ordinary Portland cement (P.O. 42.5 N), local river sand (fineness modulus of 2.3), graphite tailings (fineness modulus of 0.9), and groundwater were used throughout the experiments. The material appearance, laser particle size distribution, and granular gradation of graphite tailings and sand are shown in Figure 1. Local stone with particle size varying between 5 mm and 40.5 mm was used as a coarse aggregate. Tables 1 and 2 list the mechanical properties of cement and chemical properties of cement, sand, and graphite tailings. Table 3 lists the mineral content of cement and graphite tailings. The physical properties of sand, graphite tailings, and coarse aggregates are listed in Table 4. In this study, the graphite tailings were replaced as sand in different volume ratios from 0% to 100%. The water-to-cement ratio (w/c) was 0.52, and the mixing proportions of GTC are listed in Table 5.

2.1.2. Specimen Casting and Curing Conditions. The GTC specimens with dimensions of 150 mm × 150 mm × 300 mm (200 specimens) and 150 mm × 150 mm × 150 mm (200 specimens) were demoulded after 24 h in accordance with the Chinese standards of GB/T 50081-2001 [27]. Each sample was placed in a steam curing room with a temperature of 24 ± 2°C and a relative humidity of 95% for different curing days (3, 7, 14, and 28 days).

2.2. Experimental Methods

2.2.1. Mechanical and Electroconductivity Property Test. A total of 200 specimens were prepared for the compressive strengths of 3, 7, 14, and 28 curing days by an electronic universal testing machine (MTS-300). The electroconductivity data are characterized by the resistivity value due to the quadrupole method under the power supply voltage of 12 V after different curing days (200 specimens).

2.2.2. Material Characterization Tests. In this paper, the material morphology of graphite tailings concrete was analyzed by *scanning electron microscopy* (*SEM*) and *atomic force microscope* (*AFM*), and the pore structure distribution was investigated by *mercury intrusion porosimetry* (*MIP*) in accordance with Chinese regulations GB/T 21650-2008 [28], GB/T 16594-2008 [29], and ISO 13095-2014 [30]. In summary, the flowchart of research and experimental method used in this paper is shown in Figure 2.

3. Results and Discussion

3.1. Macroscopic Property Analysis of GTC

3.1.1. Compressive Strength of GTC. The substitution rate of graphite tailings in concrete is 0% to 100% (in volume percentage), and the mechanical properties are shown in Figure 1. The volume replacement rate in the range of 10% to 20% has a positive effect on the improvement of concrete mechanical properties. When the replacement ratio of GT is 10%, the compressive strength is 42.27 MPa (achieved maximum) with a growth rate of 14.9%. Simultaneously, the mechanical properties of concrete (GT > 20%) decline in volatility (shown in Figures 3 and 4). When the replacement ratio was 80%, the compressive strength decreased by 27.1%. Within 10% to 20% of replacement, GT has a positive improvement in the mechanical properties of concrete. The preliminary interpretation reason is as follows: (1) The necessity of ultrafine aggregate results. From the perspective of volume filling and space replenishment, a certain amount of ultrafine aggregate can improve the macroscopic properties of the material. Because the fineness of GT is 61% lower than that of sand, it is better to form a stronger cementitious medium when the amount is substituted, which provides a guarantee for the composition of the concrete skeleton. (2) However, the superfine aggregate has a large water absorption rate and insufficient particle size distribution, resulting in a threshold for its replacement rate (addition amount). The aggregate stability and the bonding capacity between aggregates in concrete are significantly reduced due to the excessive introduction of graphite tailings. When the replacement ratio exceeds 20%, it can significantly inhibit the development of compressive strength of concrete. Therefore, considering the strength and design requirements of building materials, this paper conducts electrical and material property analysis from GTC-0 to GTC-40.
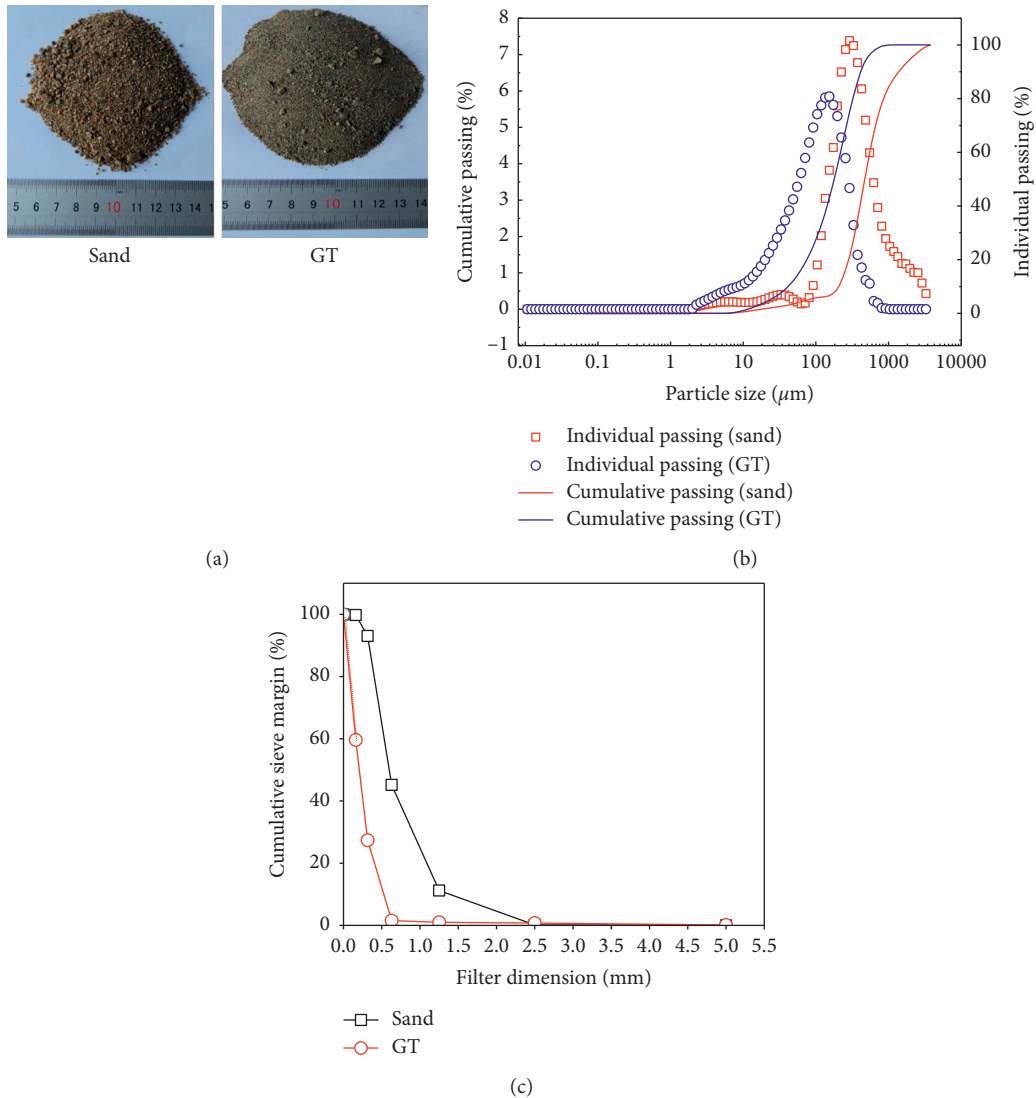
(a)

(b)

(c)

Figure 1: (a) Material appearance, (b) particle size distribution, and (c) granular gradation of GT and sand.

3.1.2. Electroconductivity and Resistivity of GTC. Concrete is currently the most used building material in the world. With the advancement of society, building materials are moving towards light, high performance, green, and intelligent. However, the traditional concrete is not an ideal conductor. The intelligence of concrete depends on the changes of conductivity or resistivity based on the influence on the incorporation of metal fibres, graphite, and metal powders. Due to the presence of a certain amount of graphite in the GT, a new type of conductive concrete can be prepared without affecting the strength. In this paper, the resistivity of GTC (0% to 40%) was investigated and is shown in Figure 5. With the gradual hydration and compaction of the matrix material, the electrical resistivity of the concrete increases in the order of magnitude, and the resistivity of GTC-0 and GTC-10 is 2.3×10^{4} and 1.8×10^{4} in loss of 18% at day 28. Graphite is an allotrope of elemental carbon. Each carbon atom is connected to another three carbon atoms in a hexagonal structure. Since each carbon atom uses three electrons to form three covalent bonds with the surrounding

carbon atom, there is one electron remaining in each carbon atom, and these electrons are free to move, so they have good conductivity. Graphite is incorporated into the concrete with GT, which forms a conductive network interconnected inside the concrete. However, as the GT content increases, the compressive strength of the incorporated concrete decreases significantly. Simultaneously, when the GT incorporation is greater than 20%, the resistivity of the concrete is not satisfactory and the high content of GT has only a certain change in the electrical resistivity of the early stage of concrete at day 3 or day 7. According to the resistivity, the conductivity of GTC was calculated and is shown in Figure 6 and the conductivity of GTC-0 and GTC-10 is 4.34×10^{-5} and 5.56×10^{-5} at day 28 with an increase of 1.22×10^{-5}. GT has an increase in the electrical conductivity of pure concrete, although this increase does not change as much as a magnitude change. However, since the concrete itself is not a conductive material, the change in the weak electrical properties can provide a possibility for the preparation of intelligent building materials in the future. Fitting

TABLE 1: Mechanical properties of Portland cement (MPa).

Flexural strength (MPa)		Compressive strength (MPa)		Fineness	Setting time (h : m)	
3 days	28 days	3 days	28 days	1.2	Initial setting	Final setting
3.3	6.9	19.2	38.5		3 : 30	4 : 19

TABLE 2: Chemical properties of Portland cement, sand, and graphite tailings (%).

Materials	Chemical compositions								
Cement	CaO	SiO_2	Al_2O_3	Fe_2O_3	MgO	SO_3	Loss		
	59.64	21.47	5.80	4.04	3.24	2.08	2.44		
GT	CaO	SiO_2	Al_2O_3	Fe_2O_3	MgO	SO_3	V_2O_5	K_2O	Loss
	15.55	62.50	10.21	5.07	2.33	0.54	0.42	2.26	1.17
Sand	SiO_2	Loss							
	99.80	0.02							

TABLE 3: Mineral content of cement and graphite tailings (%).

Cement	C_3S	C_2S	C_4AF	C_3A	Gypsum	Semiwater gypsum	Impurities
	65.70	18.10	8.50	4.70	2.10	0.20	0.07
Graphite tailings	Hematite	Clay	Plagioclase	Quartz	Black mica	Impurities	LOI
	1.10	7.40	41.40	38.30	8.60	3.20	4.15

TABLE 4: Properties of sand, graphite tailings, and stone.

Physical properties	Fine aggregate	Fine aggregate	Coarse aggregate
Type	Natural stand	Graphite tailings	Crushed stone
Size (mm)	0.16–5	0.2–0.4	5–40.5
Apparent density (kg/m^3)	2,620	2,855	2,650
Bulk density (kg/m^3)	1,630	1,540	1,550
24-hour water absorption (%)	16.80	37.10	2.17
Fineness modulus	2.49	0.90	—
pH value	7.00	10.00	7.30

TABLE 5: Mixing proportions of GTC 0% to 100% (kg/m^3).

W/C = 0.52	Replacement volume (%)	Cement (kg·m^{-3})	River sand (kg·m^{-3})	GT (kg·m^{-3})	Coarse aggregate (kg·m^{-3})	Water (kg·m^{-3})	Admixture (kg·m^{-3})
GTC-0	0	346.15	550.33	0.00	1284.10	180.00	1.04
GTC-10	10	346.15	495.27	59.97	1284.10	18.00	1.04
GTC-20	20	346.15	440.24	119.94	1284.10	180.00	1.04
GTC-30	30	346.15	385.21	179.91	1284.10	180.00	1.04
GTC-40	40	346.15	330.18	239.88	1284.10	180.00	1.04
GTC-50	50	346.15	275.15	299.85	1284.10	180.00	1.04
GTC-60	60	346.15	220.12	359.81	1284.10	180.00	1.04
GTC-70	70	346.15	165.09	419.78	1284.10	180.00	1.04
GTC-80	80	346.15	110.06	479.75	1284.10	180.00	1.04
GTC-90	90	346.15	55.03	539.72	1284.10	180.00	1.04
GTC-100	100	346.15	0.00	599.69	1284.10	180.00	1.04

relationship between resistivity and compressive strength of GTC at day 28 is shown in Figure 7.

3.2. Material Property Analysis of GTC. In order to further explore the modification mechanism of GT on concrete

compressive strength and electrical resistivity, this paper conducted a mesoexperimental analysis of GTC-0 to GTC-40.

3.2.1. Material Feature Analysis of GTC. Variations in the material features of GTC (solid samples) are shown in
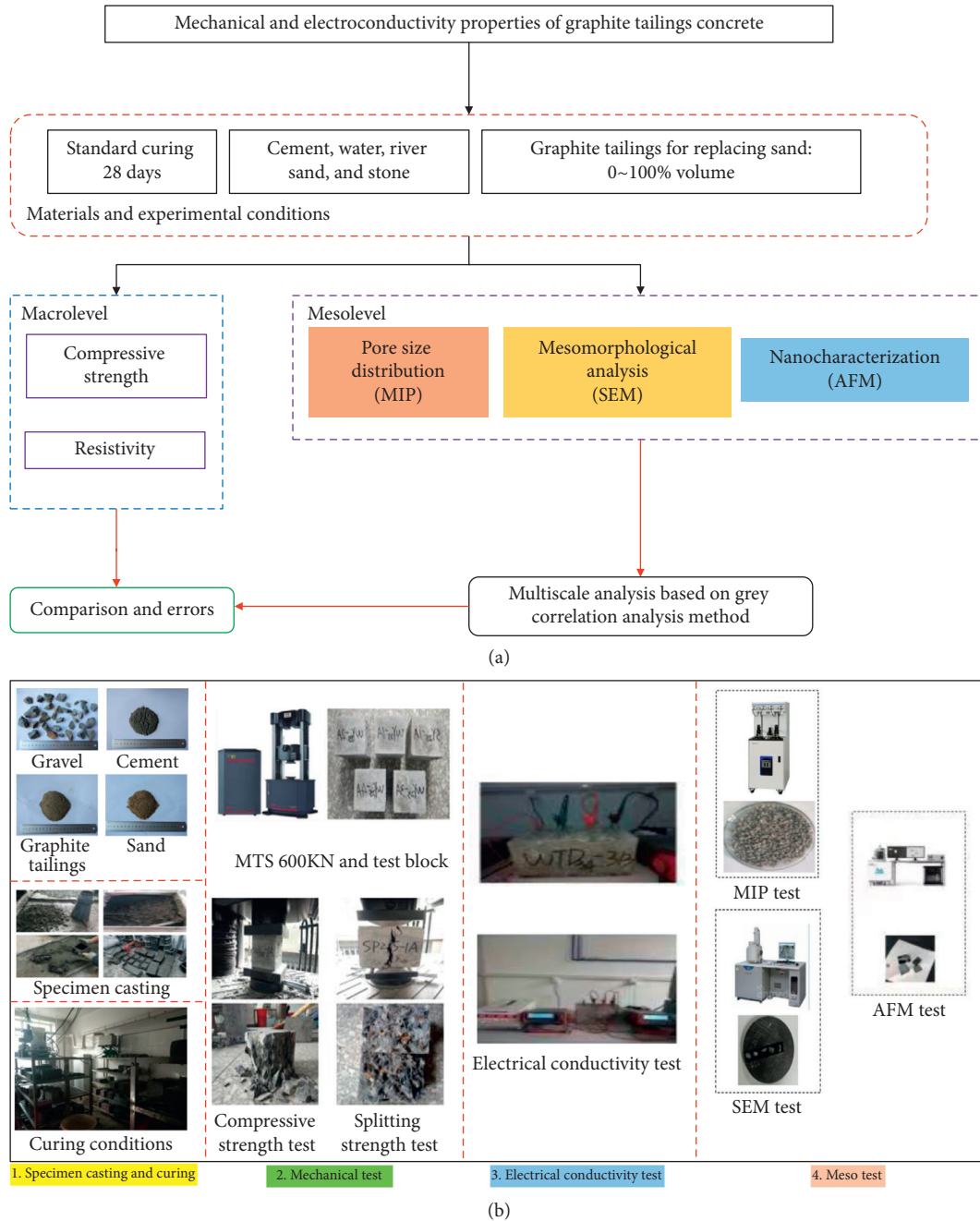
Figure 2: (a) Research flowchart and (b) experimental flowchart.

Figure 8. With the increasing amount of GT incorporation, the hydration product appears in the dense cluster form. 10% of GT addition will improve the hydration process of the cement-based material and be conducive to the growth of hydration products. However, when the GT amount is from 20% to 40%, the mesoscopic characteristics of GTC exhibit more pore structure, microcracks, and needle-like products because the high water absorption of GT leads to insufficient hydration, which affects the macrostrength performance. In order to further observe the effect of the amount of GT incorporated on the GTC hydration product, SEM analysis was performed by grinding the GTC solid into a powder. The mesoscopic features of GTC (power) are shown in Figure 9; the 10% addition of GT is advantageous for the formation of flocculent C-S-H gels and the aggregation of the C-S-H gel which is beneficial to the full hydration of the cement-based material.

3.2.2. Mesoscopic Feature Analysis of GTC. In this study, nanoscale characterization of GTC was performed by AFM and is shown in Figures 10 and 11. The surface of the cement-based material changes from rough to flat (with a sheet or
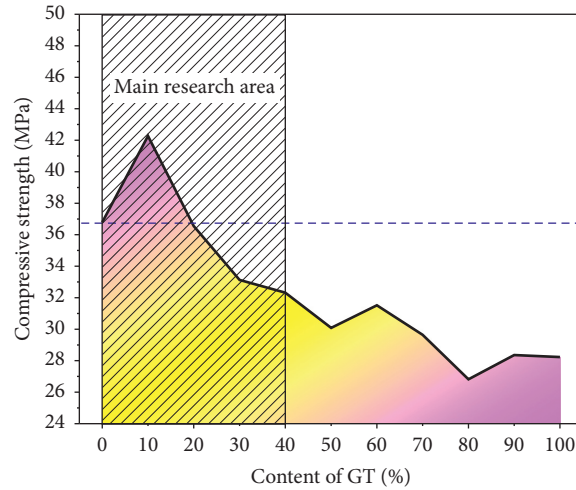
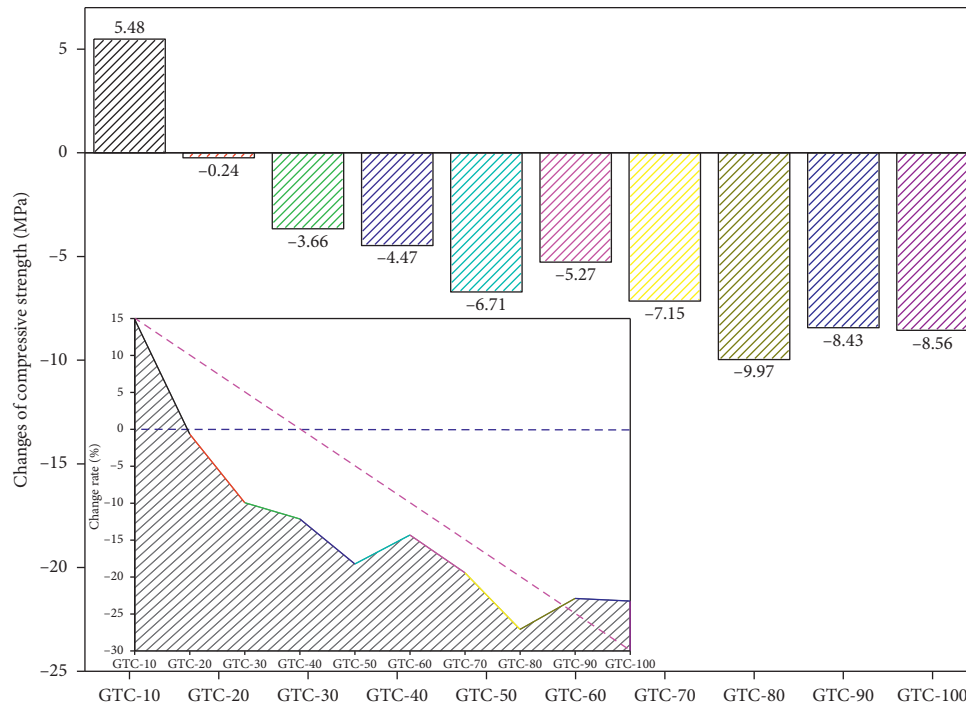FIGURE 3: Compressive strength of GTC (0% to 100%).

FIGURE 4: Changes of compressive strength of GTC (0% to 100%).

granular product) with the increase of GT amount, and the surface has some uneven areas such as valley or gully regions due to the insufficient degree of hydration. The max values of topography vs. distance of GTC-0 to GTC-40 are 13.6 nm (appeared in the 2.87 μm), 2.3 nm (appeared in the 0.51 μm), 8.1 nm (appeared in the 0.22 μm), 3.8 nm (appeared in the 2.87 μm), and 4.9 nm (appeared in the 2.87 μm). GT's own ceramic material properties play a role in the nano-modification of cement-based materials. The proper amount of GT is beneficial to the optimization of the surface morphology and morphology and surface roughness of the matrix

gel in cement-based materials. Simultaneously, graphite particles present in GT increase the roughness of the matrix and increased roughness is detrimental to the propagation of electrical signals. The results of AFM experiments were quantified by gradation histograms and are shown in Figure 12. GT has an increasing effect on the grayscale value of GTC roughness and the largest one is in GTC-40.

3.2.3. Evolution of Pore Structure of GTC. In this paper, the pore structure characteristics of GTC are shown in
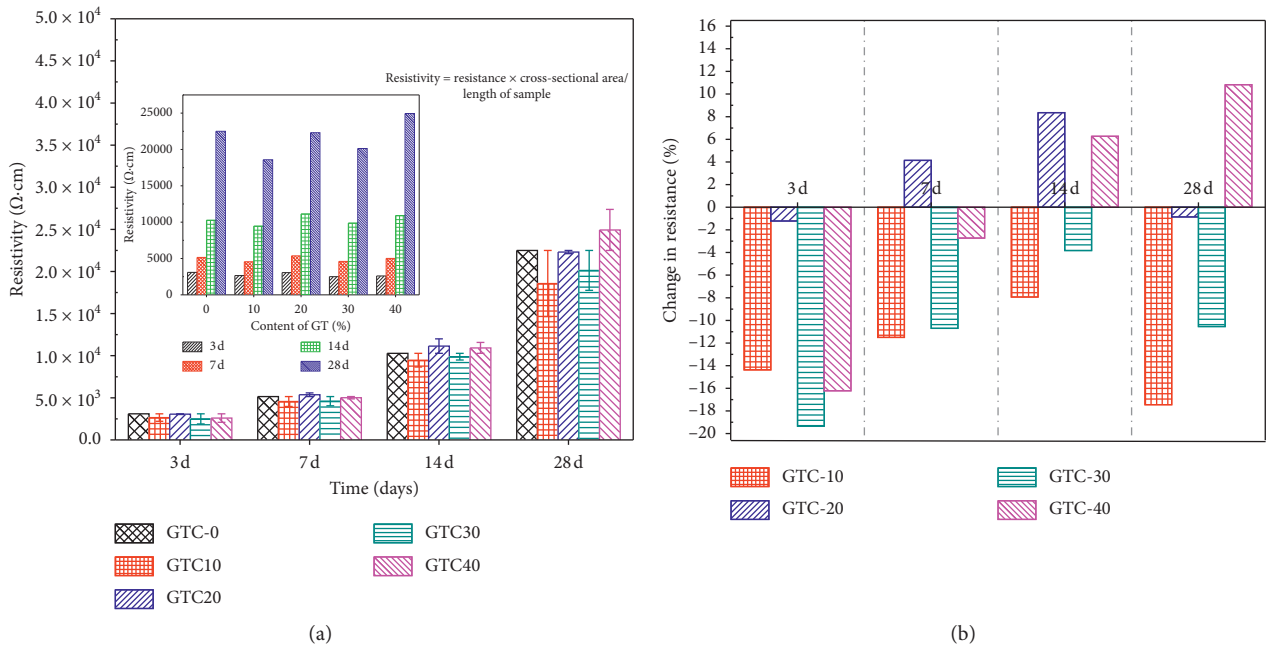
(a)

(b)

Figure 5: Resistivity properties of GTC (0% to 40%) in different curing days.
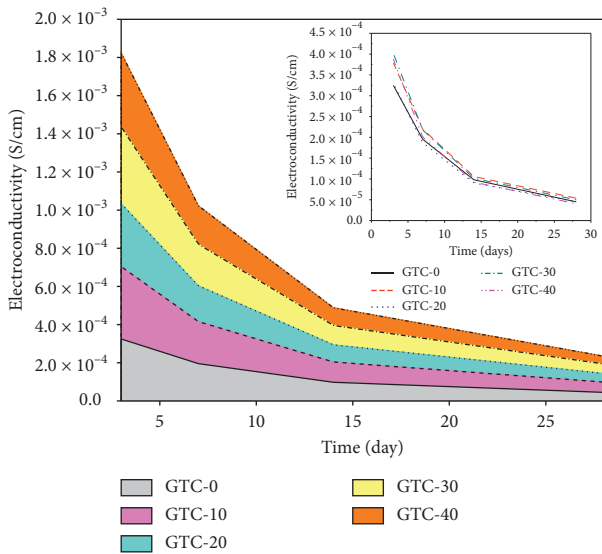

Figure 6: Electroconductivity of GTC (0% to 40%) in different curing days.

Figure 7: Relationship between compressive strength and resistivity of GTC (0% to 40%).

Figure 13. The peak value of the pore size distribution of GTC-10 was the lowest and that of GTC-40 was the highest. The area integral values of the MIP curves decreased from 1879.64 mL·nm/g to 1722.58 mL·nm/g and increased to 2150.85 mL·nm/g. This trend implies that the pore structure of GTC becomes unstable with the increase in the content of graphite tailings. The porosity, median pore size, average pore size, most probable pore size, and total pore area with different contents of graphite tailings are shown in Table 6. The porosity of GTC-0 to GTC-40 changed from 18.6% to 16.4% and increased to 22.6%, and the total pore area
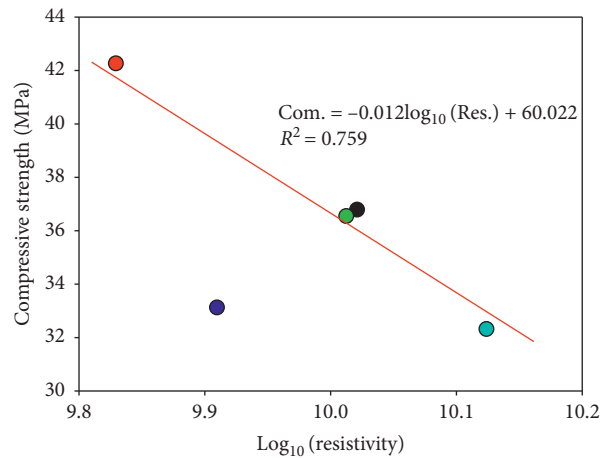
decreased from 20.5 m^2/g to 17.8 m^2/g and increased to 25.2 m^2/g. The median pore size, average pore size, and most probable pore size decreased from 28.7 nm to 22.0 nm, 19.3 nm to 18.8 nm, and 9.1 nm to 8.0 nm and increased to 27.9 nm, 19.8 nm, and 21.1 nm, respectively. When comparing the results of the pore sizes for GTC-0 and GTC-10, more small-diameter pores were observed as the content of graphite tailings increased because of the filling of graphite tailings, which led to the densification of the matrix.

The development of mesostructure and formation of the microstructure of cement-based materials directly affect the macroscopic properties such as compressive strength, workability, durability, electroconductivity, and fire resistance and characterization [31–41]. In particular, the pore
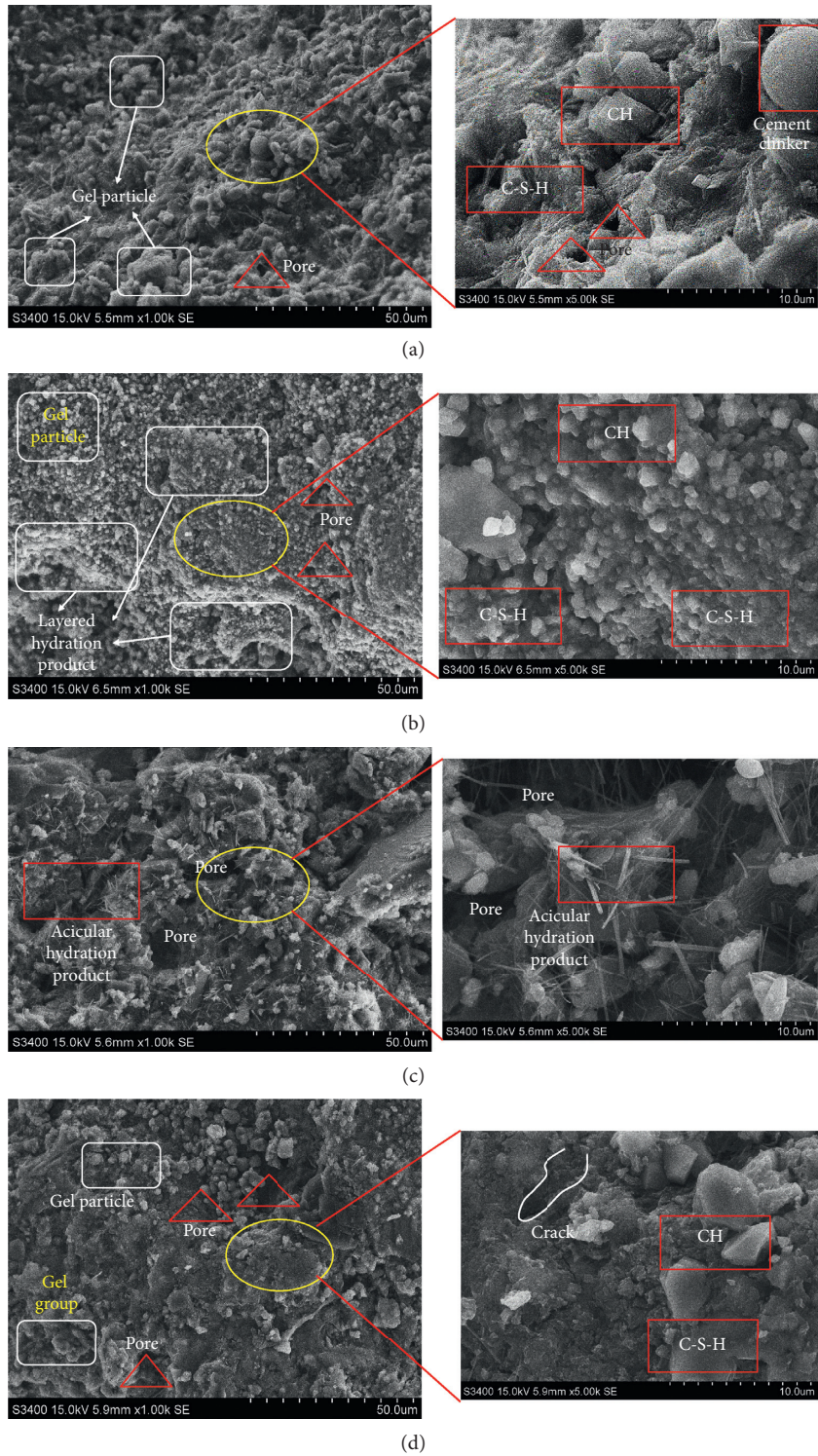
(a)

(b)

(c)

(d)

Figure 8: Continued.

(e)

FIGURE 8: Mesomorphological and mineral crystal analysis of GTC (0% to 40%) based on SEM (solid, 1.0 k to 5.0 k). (a) GTC-0; (b) GTC-10; (c) GTC-20; (d) GTC-30; (e) GTC-40.

(a)
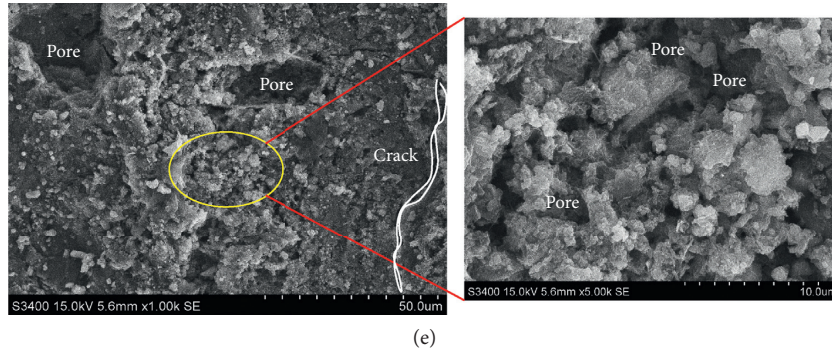

(b)

(c)

FIGURE 9: Continued.

(d)

(e)

FIGURE 9: Mesomorphological and mineral crystal analysis of GTC (0% to 40%) based on SEM (power, 1.0 k to 5.0 k). (a) GTC-0; (b) GTC-10; (c) GTC-20; (d) GTC-30; (e) GTC-40.
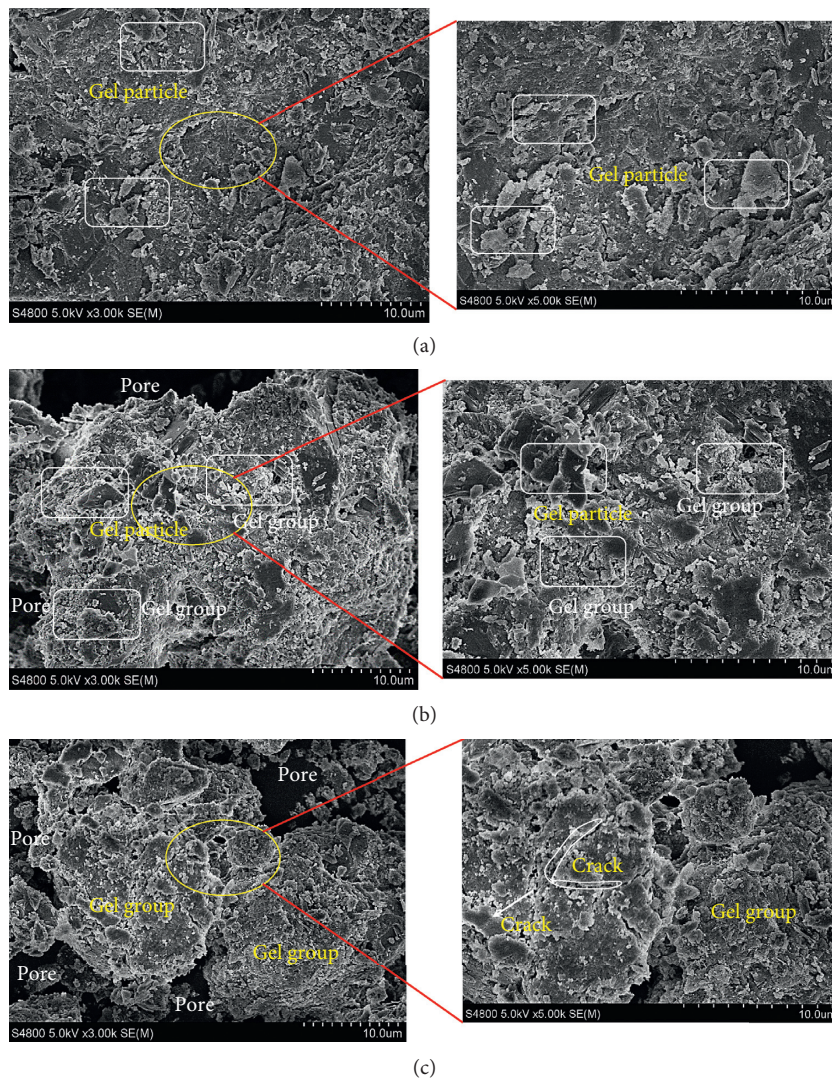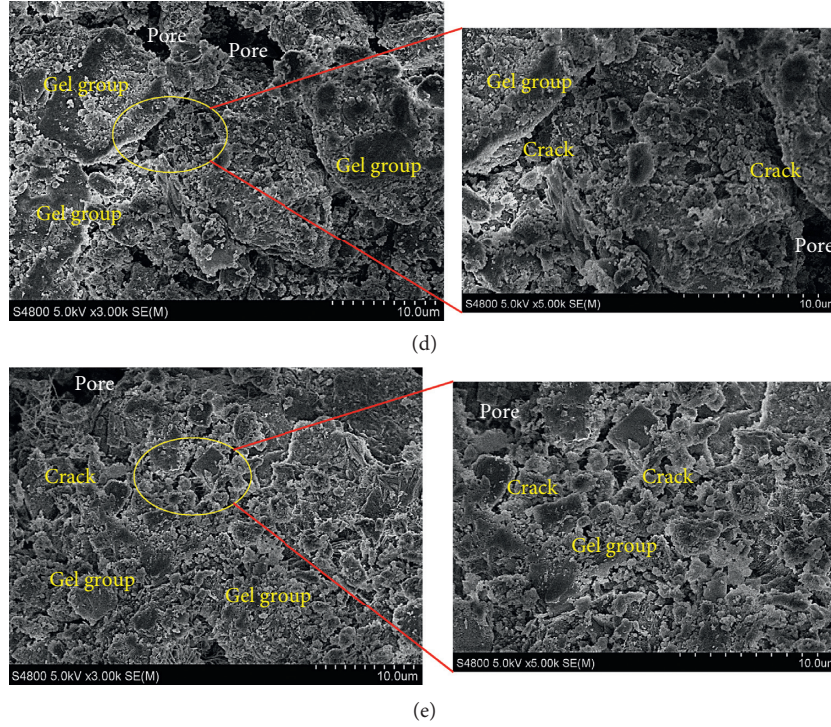
structure has a significant influence on the strength and durability of the cement-based material. At the same time, the addition of different contents of admixture (instead of cement or fine aggregate) has important modifications and effects on the nanoscale characteristics of cement-based materials [42, 43]. In this paper, the graphite-tailed ore is used to replace the fine aggregate to make the cement-based material. Based on the multiscale method, the influence equation of the different graphite tailings on the pore structure of the cement-based material, which is related to the distribution of pore sizes and porosity, was established according to the inhomogeneity effect of graphite tailings. The pore size in different contents of GT was established as follows:

$$R_i(\varphi) = a_i f(\varphi), \tag{1}$$

where $R_i(\varphi)$ is the different types of pore size such as median pore size, average pore size, most probable pore size, or others with different GT contents, φ is the GT contents, a_i is the fitting factors, and $f(\varphi)$ is the relationship equation of GT contents.

The porosity of cement-based materials with different contents of GT was defined as follows:

$$P_{R_i}(\varphi) = b_j \cdot \frac{\sum_{R_0}^{R_i} (4/3)\pi (R_i)^2}{V_{\text{GTC}}} \cdot [A_w], \quad [A_w] = H \times \frac{[W]^m}{[GTC]^m}, \tag{2}$$

where $P_{R_i}(\varphi)$ is the porosity with different GT contents, V_{GTC} is the volume of GTC, b_j is the fitting factor, $[A_w]$ is the combined water coefficient, H is the hydration degree, $[W]^m$

is the mass of water, and $[GTC]^m$ is the mass of GTC specimen.

The calculation and experimental values of pore size and porosity based on equations (1) and (2) are shown in Figure 14. As shown in Figure 13, the calculation results of the pore structure characteristics are in favourable agreement with the experimental results.

3.3. Relationship between GTC Mechanics and Resistivity according to the Grey Correlation Method.
In Section 3.1.2, the relationship between the compressive strength of GTC and the resistivity is determined by the fitting method. However, the established relationship equation has low correlation and fitness, which need to be improved. This paper chooses the grey relational degree method and proposes a new relational computing model.

Grey correlation method is a multifactor statistical analysis method. It uses grey correlation degree to describe the strength, size, and order of the relationship between the factors based on the sample data of each factor [44–46]. The grey correlation method is a significant tool for data fitting and data correlation analysis in engineering, economics, and data processing [47–49]. A multiscale relational model for the eigenvalues of pore structure and the macroscopic properties of cement-based materials was established based on the grey correlation method. The flowchart of this calculation method is shown in Figure 15. The correlation degree between the eigenvalues of the pore structure and the macroscopic properties of the GTC was determined as follows:

(a)

(b)

(c)

(d)

(e)

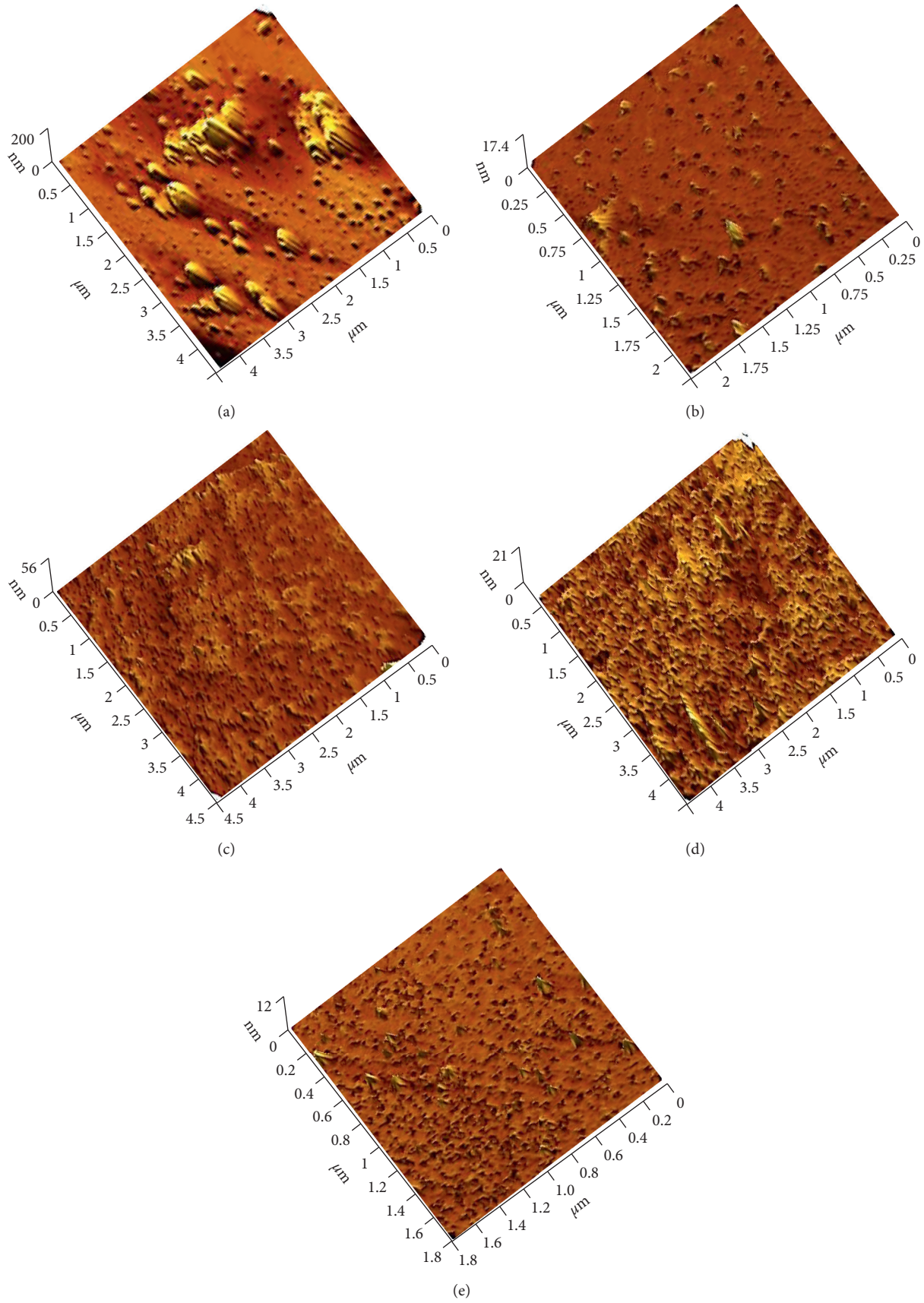FIGURE 10: AFM analysis of GTC (0% to 40%). (a) GTC-0; (b) GTC-10; (c) GTC-20; (d) GTC-30; (e) GTC-40.
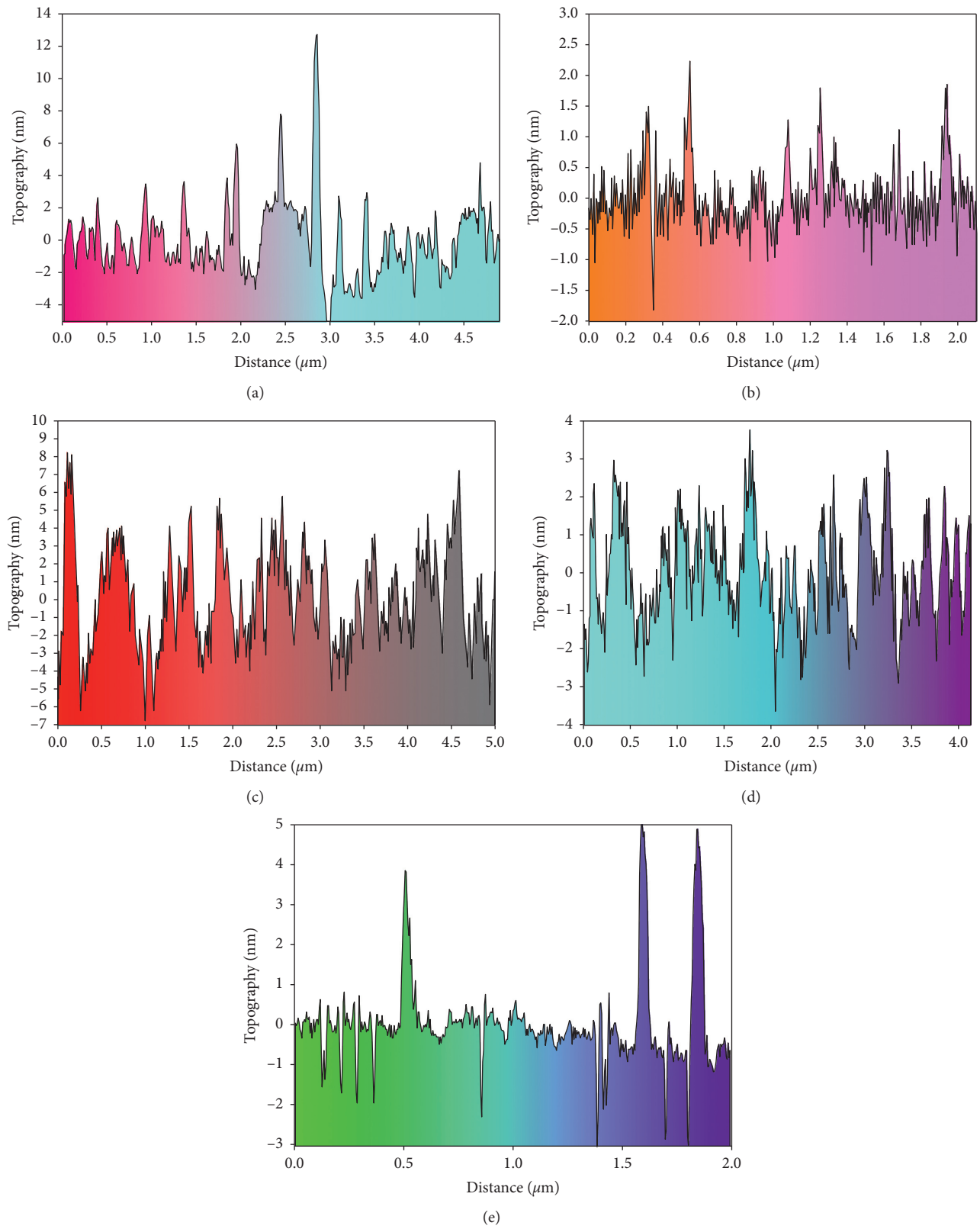
(a)

(b)

(c)

(d)

(e)

FIGURE 11: Topography vs. distance analysis of GTC (0% to 40%). (a) GTC-0; (b) GTC-10; (c) GTC-20; (d) GTC-30; (e) GTC-40.
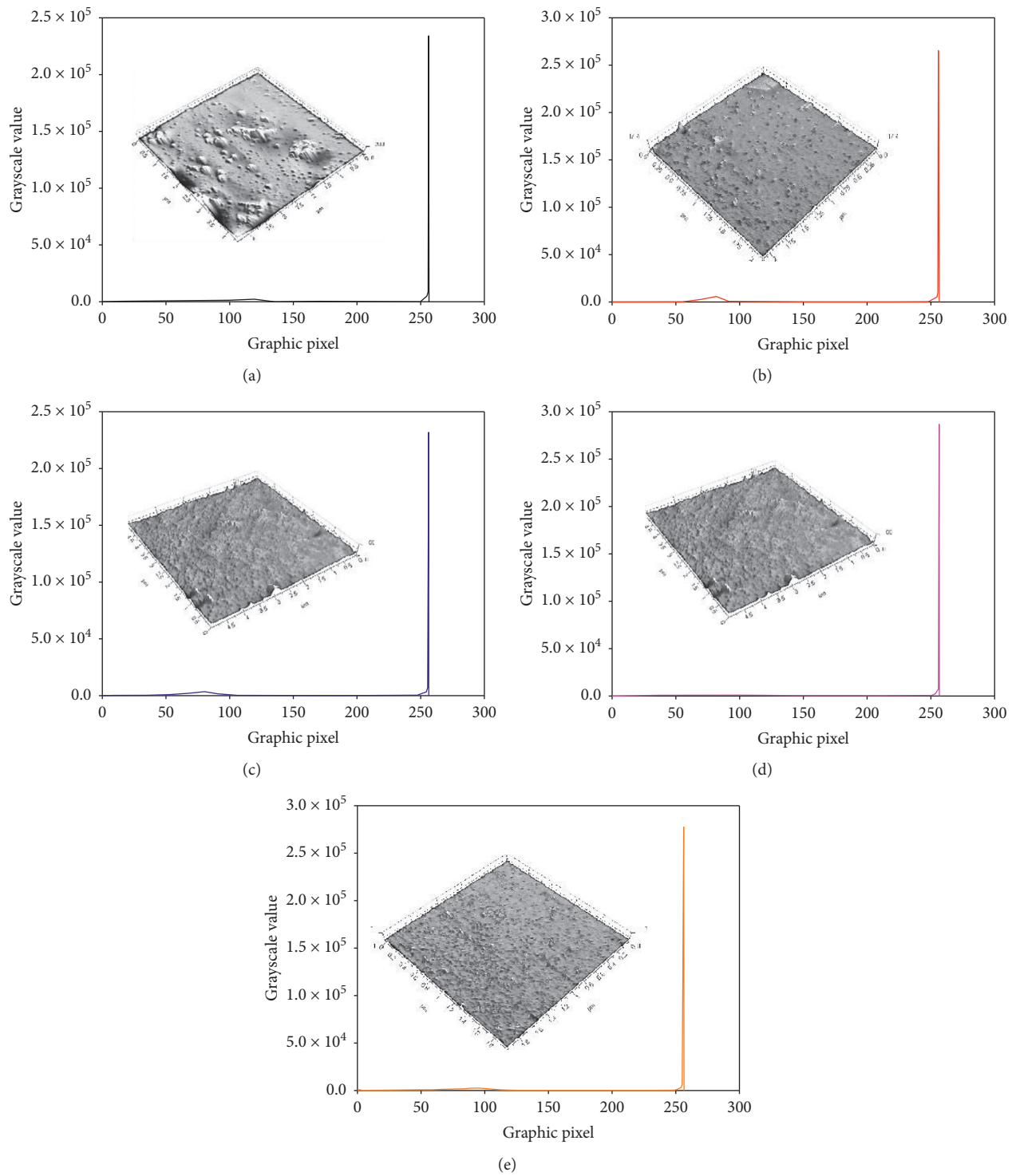
(a)

(b)

(c)

(d)

(e)

FIGURE 12: Grayscale analysis on AFM results of GTC (0% to 40%). (a) GTC-0; (b) GTC-10; (c) GTC-20; (d) GTC-30; (e) GTC-40.
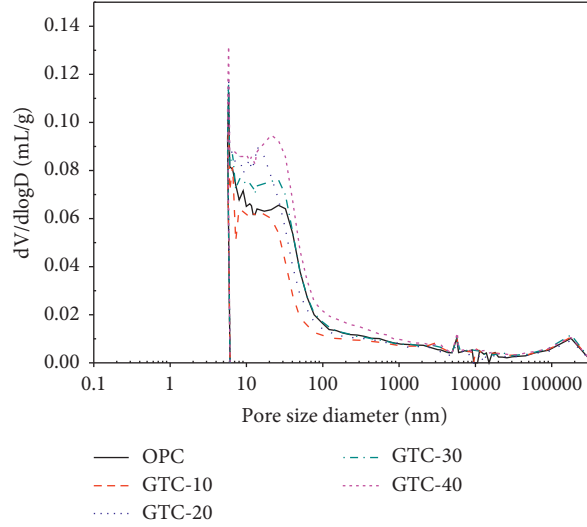
FIGURE 13: Pore size distribution of GTC (0% to 40%).

TABLE 6: Pore structure characteristics of GTC 0% to 40%.

Test piece number	Porosity (%)	Median pore size (nm)	Average pore size (nm)	Most probable pore size (nm)	Total pore area (m^2/g)
GTC-0	18.6	28.7	19.3	9.7	20.5
GTC-10	16.4	25.0	18.8	8.0	17.8
GTC-20	19.3	22.0	17.6	11.1	23.2
GTC-30	19.9	27.3	19.3	13.7	21.8
GTC-40	22.6	27.9	19.8	21.1	25.2

Step 1. Establish compressive strength row matrix A and resistivity row matrix B with pore structure characterization:

$$\mathbf{A} = \left\{ [\mathbf{Com}(\boldsymbol{\varphi})]', [\mathbf{R_i}(\boldsymbol{\varphi})]', [\mathbf{P_{R_i}}(\boldsymbol{\varphi})]' \right\}_n$$

$$= \begin{bmatrix} (\mathrm{Com}(\varphi))_0 & (\mathrm{Com}(\varphi))_1 & \cdots & (\mathrm{Com}(\varphi))_n \\ (R_i(\varphi))_0 & (R_i(\varphi))_1 & \cdots & (R_i(\varphi))_n \\ (P_{R_i}(\varphi))_0 & (P_{R_i}(\varphi))_1 & \cdots & (P_{R_i}(\varphi))_n \end{bmatrix},$$

$$\mathbf{B} = \left\{ [\mathbf{Ele}(\boldsymbol{\varphi})]', [\mathbf{R_i}(\boldsymbol{\varphi})]', [\mathbf{P_{R_i}}(\boldsymbol{\varphi})]' \right\}_n$$

$$= \begin{bmatrix} (\mathrm{Ele}(\varphi))_0 & (\mathrm{Ele}(\varphi))_1 & \cdots & (\mathrm{Ele}(\varphi))_n \\ (R_i(\varphi))_0 & (R_i(\varphi))_1 & \cdots & (R_i(\varphi))_n \\ (P_{R_i}(\varphi))_0 & (P_{R_i}(\varphi))_1 & \cdots & (P_{R_i}(\varphi))_n \end{bmatrix}$$

(3)

where $\mathbf{A}$ is the compressive strength row matrix with pore size and porosity, $\mathbf{B}$ is the resistivity row matrix with pore size and porosity, $[\mathbf{Com}(\boldsymbol{\varphi})]'$ is the compressive strength row matrix, $[\mathbf{Ele}(\boldsymbol{\varphi})]'$ is the resistivity row matrix, $[\mathbf{R_i}(\boldsymbol{\varphi})]'$ is the pore size row matrix, $[\mathbf{P_{R_i}}(\boldsymbol{\varphi})]'$ is the porosity row matrix, $(\mathrm{Com}(\varphi))_0$ is the variable of compressive strength matrix, $(\mathrm{Ele}(\varphi))_0$ is the variable of resistivity matrix, $(R_i(\varphi))_0$ is the variable of pore size matrix, and $(P_{R_i}(\varphi))_0$ is the variable of porosity matrix.

Step 2. Dimensionless processing of $\mathbf{A}$ and $\mathbf{B}$ matrices:

$$\mathbf{A}' = \begin{bmatrix} 1 & \dfrac{(\mathrm{Com}(\varphi))_1}{(\mathrm{Com}(\varphi))_0} & \cdots & \dfrac{(\mathrm{Com}(\varphi))_n}{(\mathrm{Com}(\varphi))_0} \\[2mm] 1 & \dfrac{(R_i(\varphi))_1}{(R_i(\varphi))_0} & \cdots & \dfrac{(R_i(\varphi))_n}{(R_i(\varphi))_0} \\[2mm] 1 & \dfrac{(P_{R_i}(\varphi))_1}{(P_{R_i}(\varphi))_0} & \cdots & \dfrac{(P_{R_i}(\varphi))_n}{(P_{R_i}(\varphi))_0} \end{bmatrix},$$

$$\mathbf{B}' = \begin{bmatrix} 1 & \dfrac{(\mathrm{Ele}(\varphi))_1}{(\mathrm{Ele}(\varphi))_0} & \cdots & \dfrac{(\mathrm{Ele}(\varphi))_n}{(\mathrm{Ele}(\varphi))_0} \\[2mm] 1 & \dfrac{(R_i(\varphi))_1}{(R_i(\varphi))_0} & \cdots & \dfrac{(R_i(\varphi))_n}{(R_i(\varphi))_0} \\[2mm] 1 & \dfrac{(P_{R_i}(\varphi))_1}{(P_{R_i}(\varphi))_0} & \cdots & \dfrac{(P_{R_i}(\varphi))_n}{(P_{R_i}(\varphi))_0} \end{bmatrix},$$

(4)

where $\mathbf{A}'$ is the compressive strength row matrix with pore size and porosity (nondimensionalization) and $\mathbf{B}'$ is the resistivity row matrix with pore size and porosity (nondimensionalization).

Step 3. Calculate the reference line and establish the difference line matrix:
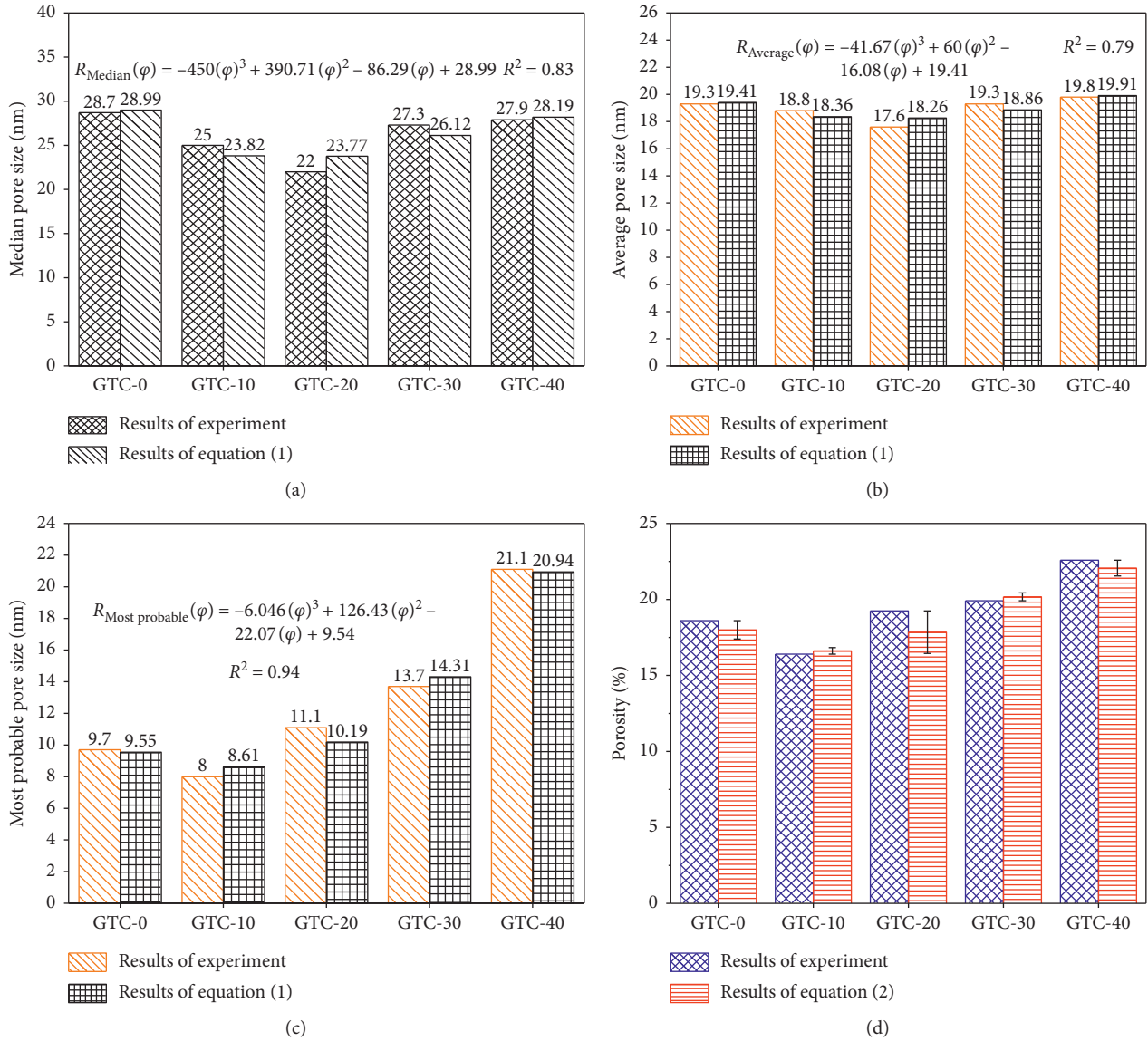
FIGURE 14: Analysis of pore structure characteristics on GTC (0% to 40%). (a) Median pore size; (b) average pore size; (c) most probable pore size; (d) porosity.

$$\mathbf{A}'\left(\mathrm{Com}\left(\varphi\right)\right) = \left[\begin{array}{cccc} 1 & \dfrac{\left(\mathrm{Com}\left(\varphi\right)\right)_1}{\left(\mathrm{Com}\left(\varphi\right)\right)_0} & \cdots & \dfrac{\left(\mathrm{Com}\left(\varphi\right)\right)_n}{\left(\mathrm{Com}\left(\varphi\right)\right)_0} \end{array}\right],$$

$$\mathbf{B}'\left(\mathrm{Ele}\left(\varphi\right)\right) = \left[\begin{array}{cccc} 1 & \dfrac{\left(\mathrm{Ele}\left(\varphi\right)\right)_1}{\left(\mathrm{Ele}\left(\varphi\right)\right)_0} & \cdots & \dfrac{\left(\mathrm{Ele}\left(\varphi\right)\right)_n}{\left(\mathrm{Ele}\left(\varphi\right)\right)_0} \end{array}\right],$$

$$\Delta\mathbf{A}' = \left[\begin{array}{cccc} 0 & \dfrac{\left(\mathrm{Com}\left(\varphi\right)\right)_1}{\left(\mathrm{Com}\left(\varphi\right)\right)_0} - \dfrac{\left(R_i\left(\varphi\right)\right)_1}{\left(R_i\left(\varphi\right)\right)_0} & \cdots & \dfrac{\left(\mathrm{Com}\left(\varphi\right)\right)_n}{\left(\mathrm{Com}\left(\varphi\right)\right)_0} - \dfrac{\left(R_i\left(\varphi\right)\right)_n}{\left(R_i\left(\varphi\right)\right)_0} \\[4mm] 0 & \dfrac{\left(\mathrm{Com}\left(\varphi\right)\right)_1}{\left(\mathrm{Com}\left(\varphi\right)\right)_0} - \dfrac{\left(P_{R_i}\left(\varphi\right)\right)_1}{\left(P_{R_i}\left(\varphi\right)\right)_0} & \cdots & \dfrac{\left(\mathrm{Com}\left(\varphi\right)\right)_n}{\left(\mathrm{Com}\left(\varphi\right)\right)_0} - \dfrac{\left(P_{R_i}\left(\varphi\right)\right)_n}{\left(P_{R_i}\left(\varphi\right)\right)_0} \end{array}\right],$$

$$\Delta\mathbf{B}' = \left[\begin{array}{cccc} 0 & \dfrac{\left(\mathrm{Ele}\left(\varphi\right)\right)_1}{\left(\mathrm{Ele}\left(\varphi\right)\right)_0} - \dfrac{\left(R_i\left(\varphi\right)\right)_1}{\left(R_i\left(\varphi\right)\right)_0} & \cdots & \dfrac{\left(\mathrm{Ele}\left(\varphi\right)\right)_n}{\left(\mathrm{Ele}\left(\varphi\right)\right)_0} - \dfrac{\left(R_i\left(\varphi\right)\right)_n}{\left(R_i\left(\varphi\right)\right)_0} \\[4mm] 0 & \dfrac{\left(\mathrm{Ele}\left(\varphi\right)\right)_1}{\left(\mathrm{Ele}\left(\varphi\right)\right)_0} - \dfrac{\left(P_{R_i}\left(\varphi\right)\right)_1}{\left(P_{R_i}\left(\varphi\right)\right)_0} & \cdots & \dfrac{\left(\mathrm{Ele}\left(\varphi\right)\right)_n}{\left(\mathrm{Ele}\left(\varphi\right)\right)_0} - \dfrac{\left(P_{R_i}\left(\varphi\right)\right)_n}{\left(P_{R_i}\left(\varphi\right)\right)_0} \end{array}\right],$$
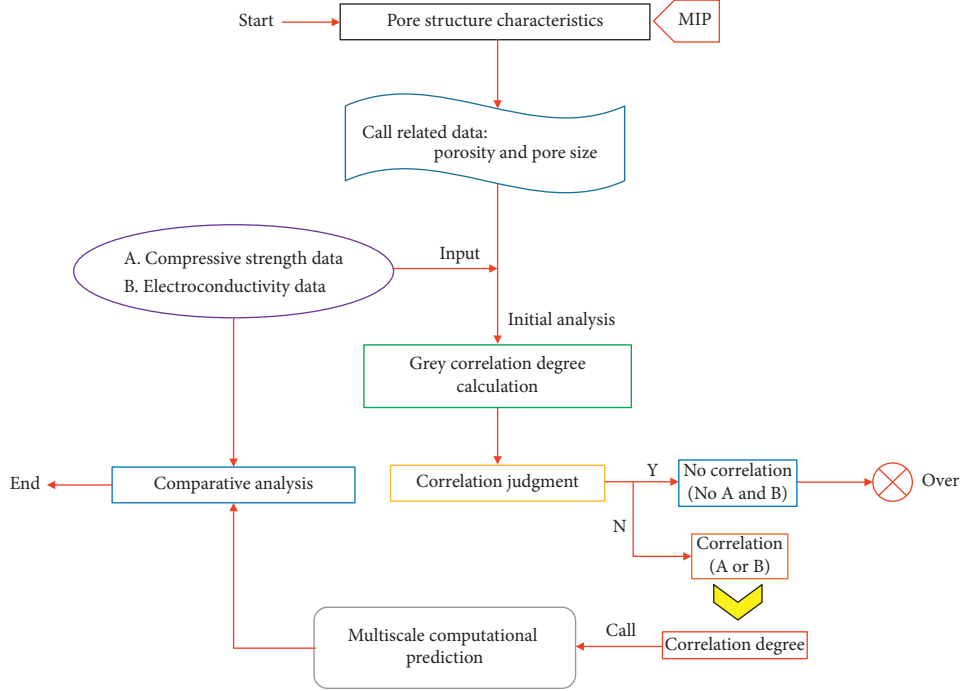
$$(5)$$

FIGURE 15: Grey correlation calculation process.

where $\mathbf{A}'\,(\mathrm{Com}\,(\varphi))$ is the calculated reference line of compressive strength row matrix with pore size and porosity (nondimensionalization), $\mathbf{B}'\,(\mathrm{Ele}\,(\varphi))$ is the calculated reference line of resistivity row matrix with pore size and porosity (nondimensionalization), and $\Delta\mathbf{A}'$ and $\Delta\mathbf{B}'$ are the difference line matrices of compressive strength and electroconductivity.

Step 4. Calculate correlation coefficient:

$$\xi_{nk}\,(\Delta\mathbf{A}') = \frac{\min_1^n\min_1^k|\Delta\mathbf{A}'| + \rho\max_1^n\max_1^k|\Delta\mathbf{A}'|}{\Delta\mathbf{A}'_k + \rho\min_1^n\min_1^k|\Delta\mathbf{A}'|},$$

$$\xi_{nk}\,(\Delta\mathbf{B}') = \frac{\min_1^n\min_1^k|\Delta\mathbf{B}'| + \rho\min_1^n\min_1^k|\Delta\mathbf{B}'|}{\Delta\mathbf{B}'_k + \rho\min_1^n\min_1^k|\Delta\mathbf{B}'|},$$

$$(6)$$

where $\xi_{nk}\,(\Delta\mathbf{A}')$ is the correlation coefficient of compressive strength row matrix with pore size and porosity (nondimensionalization), $\xi_{nk}\,(\Delta\mathbf{B}')$ is the correlation coefficient of resistivity row matrix with pore size and porosity (nondimensionalization), and ρ is the resolution coefficient, which is usually equal to 0.5.

Step 5. Calculate correlation degree:

$$r\langle\Delta\mathbf{A}'\rangle = \frac{1}{N}\sum_{k=1}^{n}\xi_{nk}\,(\Delta\mathbf{A}') \cdot r\langle\Delta\mathbf{B}'\rangle = \frac{1}{N}\sum_{k=1}^{n}\xi_{nk}\,(\Delta\mathbf{B}'),$$

$$(7)$$

where $r\langle\Delta\mathbf{A}'\rangle$ is the correlation degree of compressive strength row matrix with pore size and porosity (nondimensionalization), $r\langle\Delta\mathbf{B}'\rangle$ is the correlation degree of

resistivity row matrix with pore size and porosity (nondimensionalization), and N is the number of associated calculation data.

Based on the preliminary analysis of the correlation degree, the most relevant set of pore structure characteristic data values is selected for establishing an estimation matrix by supposing that the system has characteristic data sequence as follows:

$$\mathbf{X}_j^{(0)}\,(k) = \begin{bmatrix} x_1^{(0)}\,(1) & x_1^{(0)}\,(2) & \cdots & x_1^{(0)}\,(k) \\ x_2^{(0)}\,(1) & x_2^{(0)}\,(2) & \cdots & x_2^{(0)}\,(k) \\ \vdots & \vdots & \ddots & \vdots \\ x_j^{(0)}\,(1) & x_j^{(0)}\,(2) & \cdots & x_j^{(0)}\,(k) \end{bmatrix},$$

$$(8)$$

where $\mathbf{X}_j^{(0)}\,(k)$ is the characteristic data sequence.

Suppose the 1-AGO sequence as

$$X_j^{(1)}\,(k) = \sum_{k=1}^{n} x_j^{(0)}\,(k), \quad j = 1, 2, \ldots, n, \qquad (9)$$

where $X_j^{(1)}\,(k)$ is the 1-AGO sequence.

Generate $X_1^{(1)}\,(k)$ nearest neighbor mean sequence $Z_1^{(1)}$ as

$$Z_1^{(1)}\,(k) = \frac{1}{2}\left[X_1^{(1)}\,(k) + X_1^{(1)}\,(k-1)\right], \quad k = 2, 3, \ldots, n,$$

$$(10)$$

where $Z_1^{(1)}\,(k)$ is the 1 mean sequence.

Then, the prediction calculation equation is determined based on GM $(1, n)$ model as follows:

TABLE 7: Most grey correlation of compressive strength of GTC 0% to 40%.

Type	GTC-0	GTC-10	GTC-20	GTC-30	GTC-40	Correlation degree
Compressive strength (MPa)	36.79	42.27	36.55	33.13	32.32	—
Porosity (%)	18.6	16.4	19.25	19.91	22.58	0.7651
Median pore size (nm)	28.7	25.0	22.0	27.3	27.9	0.7411
Average pore size (nm)	*19.3*	*18.8*	*17.6*	*19.3*	*19.8*	*0.8186*
Most probable pore size (nm)	9.7	8.0	11.1	13.7	21.1	0.5371
Total pore area	20.5	17.8	23.2	21.8	25.2	0.7358

Note: values in italics indicate the highest correlation.

TABLE 8: Most grey correlation of resistivity of GTC 0% to 40%.

Type	GTC-0	GTC-10	GTC-20	GTC-30	GTC-40	Correlation degree
Resistivity value ($\Omega\cdot$cm)	22495.893	18570.065	22303.266	20124.508	24931.015	—
Porosity (%)	*18.6*	*16.4*	*19.25*	*19.91*	*22.58*	*0.8950*
Median pore size (nm)	28.7	25.0	22.0	27.3	27.9	0.8678
Average pore size (nm)	19.3	18.8	17.6	19.3	19.8	0.8416
Most probable pore size (nm)	9.7	8.0	11.1	13.7	21.1	0.7573
Total pore area	20.5	17.8	23.2	21.8	25.2	0.7950

Note: values in italics indicate the highest correlation.

$$x_1^{(0)}(k) + qZ_1^{(1)}(k) = \sum_{j=2}^{N} g_{i-1} x_j^{(1)}(k), \qquad (11)$$

$$\hat{x}_1^{(1)}(k+1) = \left[x_1^{(0)}(1) - \frac{1}{\hat{q}} \sum_{j=2}^{n} \hat{g}_{j-1} x_j^{(1)}(k+1) \right] e^{-\hat{q}k} \\ + \frac{1}{\hat{q}} \sum_{j=2}^{n} \hat{g}_{j-1} x_j^{(1)}(k+1), \qquad (12)$$

where q is called the development coefficient, g_{i-1} is called the driving coefficient, and $g_{i-1} x_j^{(1)}(k)$ is called the driving term.

Formula (12) is reduced and the grey prediction model of the original sequence is as follows:

$$\text{compressive strength: } \hat{x}_1^{(0)}(\mathbf{A}, k+1) = \hat{x}_1^{(1)}(\mathbf{A}, k+1) \\ - x_1^{(1)}(\hat{\mathbf{A}}, k), \qquad (13)$$

$$\text{resistivity: } \hat{x}_1^{(0)}(\mathbf{B}, k+1) = \hat{x}_1^{(1)}(\mathbf{B}, k+1) - \hat{x}_1^{(1)}(\mathbf{B}, k), \qquad (14)$$

where q is called the development coefficient, g_{i-1} is called the driving coefficient, and $g_{i-1} x_j^{(1)}(k)$ is called the driving term.

Finally, the relationship between the compressive strength and resistivity of GTC is determined as follows:

$$F\left[\hat{x}_1^{(0)}(\mathbf{A}, k+1) \right] = \hat{\mathfrak{I}} \cdot \hat{x}_1^{(0)}(\mathbf{B}, k+1), \qquad (15)$$

where $\mathfrak{I}$ is called the correlation coefficient.

The compressive strength and resistivity properties of GTC based on equations (13) and (14) are shown in Tables 7 and 8. The comparisons and analyses on the compressive strength and electroconductivity properties of GTC based on the multiscale model and experimental data were carried out and are shown in Figure 16. The calculated values of compressive strength are larger for the experimental results of GTC-10 and GTC-40 and smaller for those of GTC-20 and GTC-30. The average error rate is 3.01% and the max error rate is 3.79%. The calculated values of resistivity properties are larger for the experimental results of GTC-10 and GTC-30 and smaller for those of GTC-20 and GTC-40. The average error rate is 6.10% and the max error rate is 10.56%. Analysis of the calculation error by the variance in probability theory is shown in Figure 16(c). It can be found that the variance distribution conforms to the bell-shaped distribution (normal distribution). The maximum variance appears when calculating the values of compressive strength and electroconductivity of GTC-30. The calculation model in this paper has positive calculation accuracy in addition to the large instability and error in calculating GTC-30. Calculation result of new relationship between compressive strength and resistivity of GTC established by grey correlation is shown in Figure 17. A better correlation between the compressive strength and the resistivity can be obtained by the grey correlation degree (correlation coefficient is 0.93).
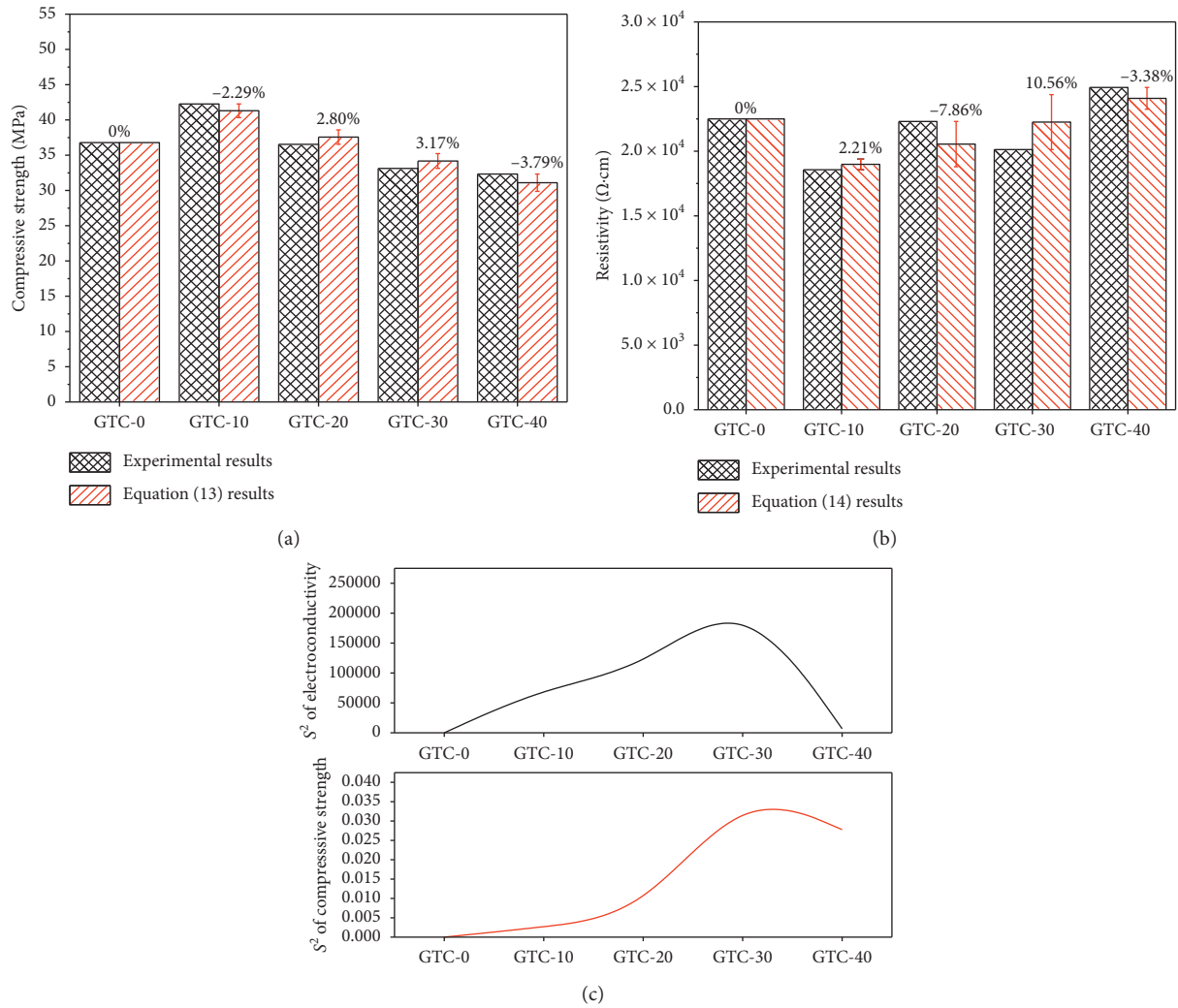
FIGURE 16: Calculation error and comparison on mechanical and resistivity properties of GTC (0% to 40%). (a) Compressive strength; (b) resistivity; (c) variance.
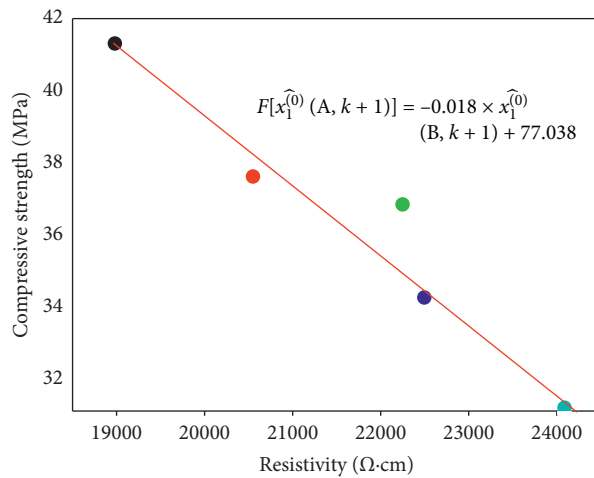

FIGURE 17: The relationship between the mechanics and resistivity of GTC based on grey correlation.

4. Conclusions

Graphite tailings are waste solids produced during the process of graphite mining, which has already caused considerable damage to the natural ecological environment. Partial replacement of graphite tailings by building sand is one of the effective ways to reuse solid waste resources. The mechanical and conductivity properties and micro- and mesoscopic structures of graphite tailings concrete have been investigated in this paper. The following conclusions can be drawn from this study:

(1) The 10% GT incorporation has a significant change in the increase of compressive strength and the decrease in resistivity of GTC.

(2) GT has an important influence on the meso-morphology, mesofolding, and pore structure of GTC. Due to the high water absorption of GT, when the amount of GT incorporated is more than 20%, the degree of hydration of GTC is suppressed, the bonding ability between coarse aggregates is lowered, and the pore structure is increased.

(3) The relationship between the mechanics and resistivity of GTC is constructed based on the grey correlation theory. This relationship can provide a theoretical basis for the preparation of green and intelligent concrete building structures through GT in the future.

Data Availability

The data used to support the findings of the study are available from the corresponding author upon request.

Conflicts of Interest

The authors declare that they have no conflicts of interest.

Authors' Contributions

Ben Li and Hongbo-Liu contributed equally to this work.

Acknowledgments

References

[1] J. Tai, M. An, and X. D. Wang, *Annual Research Report on the Development of Urban Environmental and Sanitation Industry in China: 2015-2016*, Shanghai Jiao Tong University press, Shanghai, China, 2017.

[2] D. Pedro, J. de Brito, and L. Evangelista, "Mechanical characterization of high performance concrete prepared with recycled aggregates and silica fume from precast industry," *Journal of Cleaner Production*, vol. 164, pp. 939–949, 2017.

[3] J. Xie, C. Fang, Z. Lu, Z. Li, and L. Li, "Effects of the addition of silica fume and rubber particles on the compressive behaviour of recycled aggregate concrete with steel fibres," *Journal of Cleaner Production*, vol. 197, pp. 656–667, 2018.

[4] R. Kurad, J. D. Silvestre, J. de Brito, and H. Ahmed, "Effect of incorporation of high volume of recycled concrete aggregates and fly ash on the strength and global warming potential of concrete," *Journal of Cleaner Production*, vol. 166, pp. 485–502, 2017.

[5] M. Henry, G. Pardo, T. Nishimura, and Y. Kato, "Balancing durability and environmental impact in concrete combining low-grade recycled aggregates and mineral admixtures," *Resources, Conservation and Recycling*, vol. 55, no. 11, pp. 1060–1069, 2011.

[6] C. Shi, Y. Li, J. Zhang, W. Li, L. Chong, and Z. Xie, "Performance enhancement of recycled concrete aggregate—a review," *Journal of Cleaner Production*, vol. 112, pp. 466–472, 2016.

[7] M. Chakradhara Rao, S. K. Bhattacharyya, and S. V. Barai, "Behaviour of recycled aggregate concrete under drop weight impact load," *Construction and Building Materials*, vol. 25, no. 1, pp. 69–80, 2011.

[8] L. Evangelista and J. de Brito, "Concrete with fine recycled aggregates: a review," *European Journal of Environmental and Civil Engineering*, vol. 18, no. 2, pp. 129–172, 2014.

[9] C. Alexandridou, G. N. Angelopoulos, and F. A. Coutelieris, "Mechanical and durability performance of concrete produced with recycled aggregates from Greek construction and demolition waste plants," *Journal of Cleaner Production*, vol. 176, pp. 745–757, 2018.

[10] A. Coutelieris, C. Lázaro, F. López-Gayarre, M. A. Serrano-López, P. Serna, and J. O. Castaño-Tabares, "Creep and shrinkage of recycled aggregate concrete," *Construction and Building Materials*, vol. 23, no. 7, pp. 2545–2553, 2009.

[11] M. Etxeberria, E. Vázquez, A. Marí, and M. Barra, "Influence of amount of recycled coarse aggregates and production process on properties of recycled aggregate concrete," *Cement and Concrete Research*, vol. 37, no. 5, pp. 735–742, 2007.

[12] L. Evangelista and J. de Brito, "Mechanical behaviour of concrete made with fine recycled concrete aggregates," *Cement and Concrete Composites*, vol. 29, no. 5, pp. 397–401, 2007.

[13] C. Medina, W. Zhu, T. Howind, M. I. Sánchez de Rojas, and M. Frías, "Influence of mixed recycled aggregate on the physical—mechanical properties of recycled concrete," *Journal of Cleaner Production*, vol. 68, pp. 216–225, 2014.

[14] A. K. Padmini, K. Ramamurthy, and M. S. Mathews, "Influence of parent concrete on the properties of recycled aggregate concrete," *Construction and Building Materials*, vol. 23, no. 2, pp. 829–836, 2009.

[15] C. Thomas, J. Setién, J. A. Polanco, P. Alaejos, and M. Sánchez de Juan, "Durability of recycled aggregate concrete," *Construction and Building Materials*, vol. 40, pp. 1054–1065, 2013.

[16] H. K. A. Al-Bayati, P. K. Das, S. L. Tighe, and H. Baaj, "Evaluation of various treatment methods for enhancing the physical and morphological properties of coarse recycled concrete aggregate," *Construction and Building Materials*, vol. 112, pp. 284–298, 2016.

[17] J. A. Bogas, J. De Brito, and D. Ramos, "Freezeethaw resistance of concrete produced with fine recycled concrete aggregates," *Journal of Cleaner Production*, vol. 115, pp. 294–306, 2015.

[18] G. Bianchini, E. Marrocchino, R. Tassinari, and C. Vaccaro, "Recycling of construction and demolition waste materials: a chemical-mineralogical appraisal," *Waste Management*, vol. 25, no. 2, pp. 149–159, 2005.

[19] F. B. Bodin and R. Hadjieva-Zaharieva, "Influence of industrially produced recycled aggregates on flow properties of concrete," *Materials and Structures*, vol. 35, no. 8, pp. 504–509, 2002.

[20] M. Bravo, J. de Brito, J. Pontes, and L. Evangelista, "Mechanical performance of concrete made with aggregates from construction and demolition waste recycling plants," *Journal of Cleaner Production*, vol. 99, pp. 59–74, 2015.

[21] M. Bravo, J. de Brito, J. Pontes, and L. Evangelista, "Durability performance of concrete with recycled aggregates from construction and demolition waste plants," *Construction and Building Materials*, vol. 77, pp. 357–369, 2015.

[22] Y. Peng, J. Zhang, J. Liu, J. Ke, and F. Wang, "Properties and microstructure of reactive powder concrete having a high content of phosphorous slag powder and silica fume," *Construction and Building Materials*, vol. 101, pp. 482–487, 2015.

[23] H. Liu, K. Liu, Z. Lan, and D. Zhang, "Mechanical and electrical characteristics of graphite tailing concrete," *Advances in Materials Science and Engineering*, vol. 2018, Article ID 9297628, 9 pages, 2018.

[24] Z.-R. Wang, B. Li, H.-B. Liu, Y.-X. Zhang, and X. Qin, "Degradation characteristics of graphite tailings cement mortar subjected to freeze-thaw cycles," *Construction and Building Materials*, vol. 234, p. 117422, 2020.

[25] B. Li, J. Xue, H. Liu, and W. Shen, "Comment on the paper of P. Kathirvel et al. [ACI Materials Journal, 115 (2018) 481–492]," *ACI Materials Journal*, vol. 115, pp. 133–136, 2019.

[26] P. Kathirvel, S.-J. Kwon, H.-S. Lee, S. Karthick, and V. Saraswathy, "Graphite ore tailings as partial replacement of sand in concrete," *ACI Materials Journal*, vol. 115, pp. 481–492, 2018.

[27] GB/T 50081-2001, Standard for Test Method of Mechanical Properties on Ordinary Concrete, 2002.

[28] GB/T. 21650-2008, Pore Size Distribution and Porosity of Solid Materials by Mercury Porosimetry and Gas adsorption. Part 1: Mercury Porosimetry, 2008.

[29] GB/T 16594-2008, General Rules for Measurement of Length in Micron Scale by SEM, 2008.

[30] ISO 13095-2014, *Surface Chemical Analysis—Atomic Force Microscopy—Procedure for in Situ Characterization of AFM Probe Shank Profile Used for Nanostructure Measurement*, International Standard Organization, Geneva, Switzerland, 2014.

[31] G. De Schutter and K. Audenaert, "Evaluation of water absorption of concrete as a measure for resistance against carbonation and chloride migration," *Materials and Structures*, vol. 37, no. 273, pp. 591–596, 2004.

[32] A. Barbudo, J. de Brito, L. Evangelista, M. Bravo, and F. Agrela, "Influence of water-reducing admixtures on the mechanical performance of recycled concrete," *Journal of Cleaner Production*, vol. 59, pp. 93–98, 2013.

[33] O. Y. Marzouk, R. M. Dheilly, and M. Queneudec, "Valorization of post-consumer waste plastic in cementitious concrete composites," *Waste Management*, vol. 27, no. 2, pp. 310–318, 2007.

[34] C. Albano, N. Camacho, M. Hernández, A. Matheus, and A. Gutiérrez, "Influence of content and particle size of waste pet bottles on concrete behavior at different w/c ratios," *Waste Management*, vol. 29, no. 10, pp. 2707–2716, 2009.

[35] K. Hannawi, S. Kamali-Bernard, and W. Prince, "Physical and mechanical properties of mortars containing PET and PC waste aggregates," *Waste Management*, vol. 30, no. 11, pp. 2312–2320, 2010.

[36] E. Rahmani, M. Dehestani, M. H. A. Beygi, H. Allahyari, and I. M. Nikbin, "On the mechanical properties of concrete containing waste PET particles," *Construction and Building Materials*, vol. 47, pp. 1302–1308, 2013.

[37] M. I. Juki, M. Awang, M. M. K. Annas et al., "Relationship between compressive, splitting tensile and flexural strength of concrete containing granulated waste Polyethylene Terephthalate (PET) bottles as fine aggregate," *Advanced Materials Research*, vol. 795, pp. 356–359, 2013.

[38] N. Saikia and J. de Brito, "Mechanical properties and abrasion behaviour of concrete containing shredded PET bottle waste as a partial substitution of natural aggregate," *Construction and Building Materials*, vol. 52, pp. 236–244, 2014.

[39] J. N. Farahani, P. Shafigh, B. Alsubari, S. Shahnazar, and H. B. Mahmud, "Engineering properties of lightweight aggregate concrete containing binary and ternary blended cement," *Journal of Cleaner Production*, vol. 149, pp. 976–988, 2017.

[40] R. S. Ravindrarajah, "Bearing strength of concrete containing polystyrene aggregate," in *Proceedings of the RILEM 8th International Conference on Durability of Building Materials and Components*, vol. 1, pp. 505–514, Vancouver, Canada, 1999.

[41] D. S. Babu, K. G. Babu, and T. H. Wee, "Properties of lightweight expanded polystyrene aggregate concretes containing fly ash," *Cement and Concrete Research*, vol. 35, no. 6, pp. 1218–1223, 2005.

[42] K. Rakesh and B. Bhatta, "Porosity, pore size distribution and in situ strength of concrete," *Cement and Concrete Research*, vol. 33, no. 1, pp. 155–164, 2003.

[43] F. Gong, Y. Wang, D. Zhang, and T. Ueda, "Mesoscale simulation of deformation for mortar and concrete under cyclic freezing and thawing stress," *Journal of Advanced Concrete Technology*, vol. 13, no. 6, pp. 291–304, 2015.

[44] J. Deng, *Grey System Fundamental Method*, Huazhong University of Science and Technology Wuhan, Wuhan, China, 1982.

[45] S. Karmakar and P. P. Mujumdar, "Grey fuzzy optimization model for water quality management of a river system," *Advances in Water Resources*, vol. 29, no. 7, pp. 1088–1105, 2006.

[46] U. Kumar and V. K. Jain, "Time series models (Grey-Markov, Grey Model with rolling mechanism and singular spectrum analysis) to forecast energy consumption in India," *Energy*, vol. 35, no. 4, pp. 1709–1716, 2010.

[47] H.-T. Pao and C.-M. Tsai, "Modeling and forecasting the CO_2 emissions, energy consumption, and economic growth in Brazil," *Energy*, vol. 36, no. 5, pp. 2450–2458, 2011.

[48] C.-S. Lin, F.-M. Liou, and C.-P. Huang, "Grey forecasting model for CO_2 emissions: a Taiwan study," *Applied Energy*, vol. 88, no. 11, pp. 3816–3820, 2011.

[49] N. M. Xie and S. F. Liu, "Discrete GM(1,1) and mechanism of grey forecasting model," *Systems Engineering-Theory & Practice*, vol. 25, no. 1, pp. 93–99, 2005.